Effect of SnS addition on the morphological and optical properties of (SnS)m (Sb 2 S 3)n nano-rods elaborated by glancing angle deposition

D. Abdelkader, F. Chaffar Akkari, N. Khemiri, R. Miloua, F. Antoni, B. Gallas, M. Kanzari

Effect of SnS addition on the morphological and optical properties of $(SnS)_m(Sb_2S_3)_n$ nano-rods elaborated by glancing angle deposition

D. Abdelkader[*1]; F. Chaffar Akkari[1]; N. Khemiri[1]; R. Miloua[2]; F. Antoni[3]; B. Gallas[4]; M. Kanzari[1,5]

[1] *Université Tunis ElManar, Ecole Nationale d'Ingénieurs de Tunis, Laboratoire de Photovoltaïque et Matériaux Semiconducteurs, BP37, 1002 Le Belvédère, Tunis, Tunisia*

[2] *Laboratoire d'Elaboration et de Caractérisation des Matériaux, Département d'Electronique, Université Djillali Liabes, BP 89, Sidi Bel-Abbés 22000, Algeria*

[3] *ICube-Laboratoire des Sciences de l'Ingénieur, de l'Informatique et de l'Imagerie, Université de Strasbourg-CNRS, 23, rue du Loess, 67037 Strasbourg Cedex, France*

[4] *Sorbonne Université, CNRS, Institut des NanoSciences de Paris, INSP, F-75005 Paris, France*

[5] *Université de Tunis, Institut Préparatoire aux Etudes d'Ingénieurs de Tunis-IPEIT, 02, Rue Jawaher Lel Nehru, 1089 Montfleury, Tunisia*

***** *Corresponding author: dhaferabdelkader@gmail.com*

Abstract

$(SnS)_m(Sb_2S_3)_n$ thin films were prepared by thermal evaporation using the glancing angle deposition technique (GLAD). The incident angle between the particle flux and the normal to the substrate was fixed at 80°. The Raman and XRD characterization revealed the amorphous character of the films due to the columnar structure as shown by the SEM characterization and AFM analysis. A strong change of the surface morphology of the films was observed and it depends on the composition. Optical properties were extracted from transmittance *T* and reflectance *R* spectra. $(SnS)_m(Sb_2S_3)_n$ thin films exhibit high absorption coefficients (10^4 - 2×10^5 cm^{-1}) in the visible range and the higher values were obtained for $Sn_3Sb_2S_6$ and it has the highest photocurrent values. The direct band gap ($E_{g\ dir}$) was in the range 2.11 – 1.67 eV. The refractive indices are calculated from optical transmittance spectra of the films. The $Sn_3Sb_2S_6$ sample exhibits a lower refractive index. All the dispersion curves of refractive index match well with the Cauchy dispersion formula and they were analyzed using Wemple-DiDomenico model. The Bruggeman effective medium approximation EMA was used to calculate the packing density of different compositions, and $SnSb_4S_7$ sample has the highest

value. The so-called Verdet coefficient was evaluated from refractive index dispersion, and it was enhanced near the band gap.

Keywords: Sn-Sb-S, GLAD, Nanostructured materials, Optical properties, morphological properties, X-ray diffraction.

1. Introduction

Glancing angle deposition (GLAD) technique has developed over the last few years. This technique is based on a physical deposition of vapor phase material on an oblique substrate with respect to the material flux. The substrate can be also moved according to two degrees of freedom (azimuthal or polar angle), as it can rotate around its axis. By acting on these parameters, nanostructures can be produced with controlled roughness and porosity [1-4]. This type of samples is in great demand to improve the sensing features of several devices. One can site the gas sensors as an example. Moreover, by governing the freedom's degrees of the substrate, it is possible to perform several shapes by the GLAD technique, such as vertical columns [5], helical [6], zigzag shapes [7], U-shaped resonators [8], and even three-armed square nanospirals [9] .

For instance, films with a porous structure have been shown to operate well in various applications such as solar cell [10], photonic crystals [11], optical filters [12], gas sensors [13] and photo-catalysis [14]. It includes metallic nanostructures of Ag nanorods that exhibit potential plasmonic properties for biomedical applications [15]. Recent researches showed combined techniques with the GLAD in order to develop certain applications, since it was technologically very successful, such as Growth Assisted by Glancing Angle Deposition (GAGLAD), which is a new technique to engineer anisotropic hybrid inorganic/organic nanostructures thin films [16]. We can also find a combination with colloidal lithography to fabricate ordered tantalum nanotopographies [17] and in another work GLAD was combined with the collimated magnetron-sputtering technique in order to tailor the refractive index of

the SiO_2 thin film [18]. Several oxides were deposited by GLAD including helical TiO_2 for perovskite solar cell application [19-21], hafnium oxide HfO_2 [22], $LiCoO_2$ nanostructured cathode for all-solid-state thin film batteries [23] and MgO for quarter-wave plates at a wavelength of 351 nm conception [24]. Aside from the oxides, chalcogenide materials class are among the materials that were performed using this technique. In a recent work, we showed optical anisotropy of $CuIn_3S_5$ and $CuIn_5S_8$ nanorods [25]. Pareek *et al.* [26] demonstrated that ZnCdS system is an efficient photoanodic material for hydrogen production. SnSe thin films exhibit enhanced thermoelectric properties when grown by pulsed laser glancing-angle deposition [27]. The effect of angle deposition of the binary materials SnS and Sb_2S_3 was studied [28,29]. Ternary chalcogenide Sn-Sb-S materials belonging to the pseudo-binary system SnS-Sb_2S_3 were not widely studied as nanostructures, and only the two phases $Sn_4Sb_6S_{13}$ and $Sn_3Sb_2S_6$ were deposited by GLAD [30,31]. These two previous works have only focused on the angle deposition effect. In the present work, we tried to investigate the effect of the variation of the chemical composition along the pseudo-binary system SnS-Sb_2S_3 on the morphological, structural and optical properties. In order to achieve this, $(SnS)_m(Sb_2S_3)_n$ nanorod thin films were elaborated by GLAD with (m:n) equal to (1:2), (2:3), (1:1), (4:3), (2:1) and (3:1).

2. Experimental details

The last combinations of SnS and Sb_2S_3 match the six following compositions $SnSb_4S_7$, $Sn_2Sb_6S_{11}$, $SnSb_2S_4$, $Sn_4Sb_6S_{13}$, $Sn_2Sb_2S_5$ and $Sn_3Sb_2S_6$. Their powders were used for thermal evaporation, from a molybdenum boat, using a high vacuum coating unit Alcatel. $(SnS)_m(Sb_2S_3)_n$ thin films were deposited at a base pressure of 10^{-6} Torr using the GLAD technique. All the films were deposited onto unheated glass substrates, which were fixed at an oblique angle of 80 °. This angle value is considered as an extremely oblique position, in

order to ensure the formation of columns. In our experiment, the deposition angle was fixed without substrate rotation.

The roughness, morphology and cross-sectional features of the samples were examined by atomic force microscope (AFM) (NT-MDT Smena) and scanning electron microscopy (SEM) (ZEISS Supra 40). The structural properties were determined by the X-ray diffraction technique using a Philips X'Pert X-ray diffractometer (40 kV, 30 mA, and CuK_α radiation λ = 0.15418 nm) in the range of 2θ = 10 – 70 ° at room temperature. Raman scattering measurements were carried out at room temperature with a Horiba Lab-RAM Aramis confocal Raman spectrometer ($\lambda_{excitation}$ = 532 nm) equipped with a cooled CCD camera and an automated XYZ table. An objective lens of 100× magnification and D3 filter were used. Transmittance and reflectance data were recorded at normal incidence with UV–Vis–NIR spectrophotometer. In order to calculate the packing density using the Bruggeman effective medium approximation (BEMA), the dielectric constant of the $(SnS)_m(Sb_2S_3)_n$ bulk materials was measured directly using UVISEL phase-modulated ellipsometer. The data measurement was performed at room temperature under a 70° incidence.

3. Results and discussion

3.1 Morphological properties

Fig. 1 shows the surface as well as the cross-section morphologies of the films. It can be seen that all the films show a columnar structure. This columnar structure results from great shadowing effect, which is enhanced for strong deposition angles, greater than 60 ° [30,31]. Obviously, the formation of this structure is strongly encouraged for an angle of 80 °. The slanted columns are highly arranged and inclined towards the evaporated material flux side.

The sorting of the materials according to the following order, $SnSb_4S_7$, $Sn_2Sb_6S_{11}$, $SnSb_2S_4$, $Sn_4Sb_6S_{13}$, $Sn_2Sb_2S_5$ and $Sn_3Sb_2S_6$ is a sorting in Sn content order. In another word, the sorting is in m/n ratio order, where m and n are the indices in the following formula

$(SnS)_m(Sb_2S_3)_n$. The taken values of m/n ratio are 1/2, 2/3, 1/1, 4/3, 2/1 and 3/1. The surface morphology shown in **Fig.1** depicts the porous structure of the films in SEM images taken at the same magnitude of 100 K×. $SnSb_4S_7$ (m/n = 1/2) sample exhibits very small and compacted nanorods, and the film seems to be dense. We note that from m/n = 1/2 to 3/1, the pores between the nanorods ends become more and more opened and the nanorods end have a larger size as can be seen in the surface morphology in SEM images. The AFM analysis comforts the observation seen in SEM images. The black surfaces shown by AFM images in **Fig.2.a** depict the hollows situated at the surfaces and show how much the films are porous. The analysis of the height distribution (**Fig.2.b**) allows determining the pores threshold and the RMS roughness value (root mean square) and we found that they increase from 6.3 to 25 nm and from 1.6 to 5.3 nm, respectively (**Table 1**). Therefore, pores become deeper with SnS content, which enhances the surface roughness. A further important observation is that the entire series of elaborated films exhibit a thickness gradient as shown in 3D AFM images in **Fig.3**, which is confirmed by SEM thickness measurement and Raman cartography. Therefore, at the top, the film is thicker. For widely oblique positions, the gradient of material flux is accentuated; the region of the substrate situated straight above the evaporation boat receives a greater flux. The diffusion on the surface is no longer the same due to this material flux gradient. Therefore, it is possible to fabricate thin films with a thickness gradient. In a previous work, tapered thickness films were elaborated using GLAD technique using a mask deposited on the substrate. The existence of the mask allows the creation of two regions; the first region is the shadowed zone of the substrate, and the second one is where the vapor flux completely reaches the substrate [32]. At the boundary of these regions, there is a small zone of thickness gradient [32]. In our experiment, the films are grown without using a mask, which is considered a technical advantage. This GLAD feature could be useful for nanophotonics and nanoelectronics applications [32].

3.2 Structural properties

The XRD patterns of $(SnS)_m(Sb_2S_3)_n$ thin films deposited with GLAD are shown in **Fig. 4 (a)**. As can be seen, there is no obvious diffraction peaks for $SnSb_4S_7$, $Sn_2Sb_6S_{11}$, $SnSb_2S_4$ and $Sn_4Sb_6S_{13}$ samples, indicating that films are amorphous. Only, the patterns of $Sn_2Sb_2S_5$ and $Sn_3Sb_2S_6$ thin films show weak peaks at 31.68° and 31.65°, respectively (JCPDS cards n° 44-0829 and 38-0826, respectively). We would note that these two compositions match with the highest values of m/n ratio.

It is well known that the glancing angle deposition technique does not conserve good crystalline features for great deposition angles [28] and in some cases the films become amorphous [33]. It was shown that Sn-Sb-S ternary materials are among these cases especially when the deposition is at room temperature [30,31]. The amorphous character of our films is due to the porous nanostructure. The void between the nanorods contributes to the amorphous behavior because we have demonstrated in a previous work that the normal deposited $(SnS)_m(Sb_2S_3)_n$ films are polycrystalline in nature, without any heat treatment [34].

In order to explain the trend of $Sn_2Sb_2S_5$ and $Sn_3Sb_2S_6$ to have a polycrystalline structure, we compared the heat of atomization H_s of these materials with each other and with the ones of its elementary compounds Sn and Sb. For ternary materials $A_xB_yC_z$, H_s is expressed as [35]:

$$H_s = \frac{xH_s^A + yH_s^B + zH_s^C}{x + y + z} \quad (1)$$

where x, y, and z are the ratios of A(Sn), B(Sb), and C(S), respectively. From the **Table 1**, it is clear that the average heat of atomization H_s increases from 275.25 to 282.18 kJ.mol^{-1} with an increase in Sn content. $Sn_2Sb_2S_5$ and $Sn_3Sb_2S_6$ have the highest values of Sn content and exist in the Sn-rich side of the pseudo-binary SnS- Sb_2S_3 system. Its atomization energies trends to the one of Sn, which is a highly crystalline metal. This is the most probable cause of the trend of $Sn_2Sb_2S_5$ and $Sn_3Sb_2S_6$ to have a polycrystalline structure. It may also be the

cause of the appreciable change of the surface morphology as it can be seen in **Fig. 1**. To consolidate this idea, we refer to the work of Sazideh *et al*. [28] on the effect of deposition angle on SnS thin films, since $Sn_2Sb_2S_5$ and $Sn_3Sb_2S_6$ are the closest compositions to SnS in the pseudo-binary system SnS-Sb_2S_3. They demonstrated that the intensity of the main XRD peaks decreased but the films were still well crystallized even at high deposition angles and without any heat treatment [28].

Fig.4 (b) shows the Raman spectra of $(SnS)_m(Sb_2S_3)_n$ films deposited by GLAD and compared with those of normally deposited films (**Fig.4 (c)**). It is clear that Raman measurements comfort the XRD results; the large bands and rough lines of the Raman spectra of $(SnS)_m(Sb_2S_3)_n$ nanorods confirm the amorphous character of the samples. Nevertheless, $Sn_2Sb_2S_5$ and $Sn_3Sb_2S_6$ films show a weak peak situated at 96 and 94 cm^{-1}, respectively, which is in accordance with XRD results. Besides, the surface state contributes to the change in the shape of the Raman spectra especially when the surface exhibits a roughness and porosity due to the columnar structure. Generally, the physical state, the morphology, thermal properties, homogeneity and pores distribution, would all be able to influence how a sample is exhibited to the Raman spectrometer [36]. The Raman spectra of highly crystallized materials resemble more closely the Raman spectra associated with their molecular crystals [37].

The effect of SnS addition is notable on the Raman spectra of the normally deposited films; the intensity of some peaks perceptibly increases, especially the one located at 94 cm^{-1} assigned to [SnS_4] tetrahedral unit [38]. This effect is not apparent in the spectra of the GLAD sample because the thickness affects the intensity and this is confirmed by Raman cartography. In other words, since the samples produced by GLAD have a thickness gradient, it is difficult to look for the same thickness for the different films, in order to make the Raman measurements. To highlight this, Raman cartography was carried out; the measurements were taken simultaneously on 10 aligned points, 10 µm apart, in the thickness gradient. For the

same wavenumber, the intensity decreases as a function of the X position on the direction of the thickness gradient (**Fig.5**).

All the Raman spectra of $(SnS)_m(Sb_2S_3)_n$ films were well fitted using seven Gaussian functions as shown in **Fig.6**. Lorentzian fit attempts fail to regenerate the experimental Raman spectra. The fitting analysis parameters of the experimental Raman spectra are summarized in **Table 2**.

3.3 Optical properties of $(SnS)_m(Sb_2S_3)_n$ films

3.3.1 Transmittance and reflectance spectra

The transmittance spectra of $(SnS)_m(Sb_2S_3)_n$ nanorods are shown in **Fig. 7 (a)**. The values are in the range 60-90 % in the transparency region and all spectra show a sharp fall at the band edge. All the transmittance spectra show loose oscillations and weak amplitude for $\lambda >$ 690 nm. Oscillations of the transmittance spectra of the normally deposited films were tighter and exhibit stronger amplitudes [34]. The amplitude decreases when the deposition angle becomes higher, and this is a well-known feature of the GLAD technique, found by other works [7,29-31]. The transmittance of $Sn_3Sb_2S_6$ sample is the highest, and the one of $SnSb_4S_7$ is the lowest. However, the reflectance varies inversely, as **Fig. 7 (a)** makes clear, $SnSb_4S_7$ sample has the highest reflectance and $Sn_3Sb_2S_6$ has the lowest one. This may be due to the surface morphologies because the confinement of light is greater when it reaches large pores. Therefore, the light trapping is enhanced.

3.3.2 Absorption coefficients and optical band gaps

The absorption coefficients α of such absorbing films can be expressed in terms of the transmittance T and reflectance R data using the relation [34]:

$$\alpha = \frac{1}{d} ln(\frac{(1-R)^2}{T}) \quad (2)$$

where d is the thickness of the film. It can be seen that the absorption coefficient α increases gradually and it exceeds 10^4 cm^{-1}. **Fig. 7 (b)** shows that all the $(SnS)_m(Sb_2S_3)_n$ films show

high absorption coefficients between 10^4 and 2×10^5 cm^{-1} in the visible range and the higher values were obtained for $Sn_3Sb_2S_6$. This is a vital outcome because semiconducting nanostructures have developed as a promising course toward accomplishing high efficiencies in photovoltaic solar cells [39]. Recently, many works demonstrated that crystalline nanostructures exhibit a high-efficiency solar cell [40,41]. The Sn-Sb-S materials do not require high annealing temperature to be crystallized, so it would be efficient to elaborate these materials as crystalline nanostructures. To obtain detailed information about the energy band gap of the samples, the dependence of the absorption coefficients α on the photon energy is analyzed in the sharp absorption region using the Tauc relation which has to date been the most popular heuristic expression, correlating the absorption coefficient and the optical band gap E_g. It can be expressed as [42]:

$$\alpha h\nu \propto \left(h\nu - E_g\right)^{\gamma} \tag{3}$$

In this relation, γ = 1/2 for a direct allowed transition or γ = 2 for an indirect allowed transition. The extrapolation to zero absorption with the photon energy axis of the linear part of $(\alpha h\nu)^2$ and $(\alpha h\nu)^{1/2}$ plots allows the determination of the direct and indirect band gaps, respectively (**Fig. 7 (c)**). $(SnS)_m(Sb_2S_3)_n$ samples exhibit direct and indirect gaps. The direct band gap ($E_{g\ dir}$) and indirect band gap ($E_{g\ ind}$) are in the range 2.11–1.67 eV and 1.87–1.42 eV, respectively and are summarized in **Table 1**. The sample $Sn_3Sb_2S_6$ (the maximum of the ratio m/n) has the lowest value of band gap energy. However, $SnSb_4S_7$ (the minimum of the ratio m/n) has the highest one. Therefore, the red shift of the band gap results from SnS addition. We note that band gap values of the samples elaborated by glancing angle deposition are higher than the ones normally deposited in a previous work [34]. The increase of the band gap value is a famous feature of the samples elaborated by GLAD technique, due to the increased disorder and porous character of the films. We have looked for the causes of gap redshift on chalcogenide materials in the literature, and we found two main reasons that are

summarized as either photo-induced change or a change in chemical composition that favors the increase of any metal content [43-46]. Consequently, the increase of the homopolar bonds between the atoms of the same metal. In order to comfort this idea, we compared with the band gap variation of a similar ternary system Ge-As-Se, where both the increase of Ge content (increase in Ge/As ratio) and UV exposure cause a reduction in E_g [47]. In our case, the SnS addition (increase in m/n ratio) increases the [SnS_4] units, and therefore increase of the homopolar bonds Sn-Sn, which causes an upward shift to the conduction band bottom.

The extinction coefficient $k = \alpha\lambda/4\pi$ reflects the amount of intensity loss of a given electromagnetic wave propagating through any medium. Therefore, the related electric field having a wavelength lower than 800 nm will be enormously dissipated (**Fig. 7 (d)**). For wavelengths higher than 800 nm, the extinction is practically null so the light wave can get through the film several times and thus interference phenomena is produced in the transparency region. This characteristic makes the samples useful for photonic devices in this spectral region. Below this region, the change in the extinction coefficient is due to the band-to-band excitation [48].

3.3.3 Some photovoltaic parameters:

Using the measured absorption coefficient $\alpha(\lambda)$, we estimated the absorbed photon fraction and photocurrent of the deposited thin films. Assuming $(SnS)_m(Sb_2S_3)_n$ based solar cell with perfect antireflection, no absorption in the upper layers and normal incidence, the thickness-dependent absorbed photon fraction and the photocurrent is calculated by the following relations [49, 50] :

$$Absorbed\ photon\ fraction = \frac{\int_{300nm}^{\lambda_g} F(\lambda)[1-\exp(-\alpha(\lambda)d)]d\lambda}{\int_{300nm}^{\lambda_g} Fd\lambda} \quad (4)$$

$$J_{ph} = e\int_{300nm}^{\lambda_g} F(\lambda)[1-\exp(-\alpha(\lambda)d)]d\lambda \quad (5)$$

where, d is the thickness (in nm), $F(\lambda)$ is the wavelength-dependent AM1.5G photon flux, e is the electron charge and λ_g=1240/E_g. In **Fig.8** we compare the performance of our thin films and show that among the six phases, $Sn_3Sb_2S_6$ exhibits the best performance with relative optical absorption very close to 97 % and photocurrent better than 32.7 mA/cm² for layer thicknesses greater than 3 µm. In addition, $SnSb_4S_7$ and $Sn_2Sb_6S_{11}$ (resp. $SnSb_2S_4$ and $Sn_4Sb_6S_{13}$) exhibit a similar photovoltaic performance.

3.3.4 Refractive indices and dispersion analysis

The refractive index n is an essential property for any optical material. It is firmly associated to the electronic polarization and the nearby field of atoms or molecules inside these materials. In this way, the knowledge of refractive index is impressively vital, particularly for the materials that can be useful for the manufacture of any optical gadgets. It can be calculated from the Swanepoel method, which requires at least two interference fringes in the transmittance spectrum [51].

Fig.9 (a) illustrates the refractive indices of $(SnS)_m(Sb_2S_3)_n$ thin films estimated using the Swanepoel method. The four terms in the Cauchy relation ($n = n_0+A/\lambda^2+B/\lambda^4+C/\lambda^6$) allow the determination of a good fit shape of the refractive index in terms of normal dispersion at very weak absorption domain (>800 nm). The Cauchy parameters are classified in **Table 3**. We note that $Sn_3Sb_2S_6$ has the lower value of refractive index n. Hence it can be concluded from this work and the two previous works [34,38] that the refractive index of $Sn_3Sb_2S_6$ is still the

smallest among those of the other five thin-film compositions, deposited on glass or on silicon or by GLAD.

The shape of the refractive indices displayed two main parts. The part I shows higher values above the absorption edge. In this part, the refractive index exhibits an abnormal dispersion behavior. This anomalous result is ascribed to the plasma frequency ω_p of the photon energy [52]. It is clear in **Fig.9 (a)** that this anomaly depends on the SnS content (m/n ratio); it appears logical since the anomalous dispersion occurs at the absorption edge. In the 2nd part (> 750 nm), the refractive index of different films $(SnS)_m(Sb_2S_3)_n$ shows a normal dispersion. A similar behavior was reported for chalcogenide materials including SnS [48], $GeSe_{2-x}Sn_x$ [53], InSe [54] and Sb_2S_3 [55]. Naturally, the SnS addition creates a bonding change and therefore a polarizability change of the material, which is directly linked to the refractive index via Lorentz- Lorenz relation. Besides, the density of the material is affected by SnS addition. The changes of the polarizability and the material density can cancel each other in such a way that refractive index remains unchanged.

In the region of normal dispersion (region II), the model proposed by Wemple and DiDomenico [56] which is a single oscillator model could be applied. In this model, the refractive index curve has been analyzed beneath the inter-band absorption edge. The energy dependence of the refractive index satisfies the following relation:

$$\frac{1}{n^2-1}=\frac{E_0}{E_d}-\frac{1}{E_0E_d}\times(h\nu)^2 \qquad (6)$$

where E_0 is the oscillator energy and E_d is the dispersion energy parameter of the material that measures the strength of inter-band optical transitions. Plots of $(n^2\text{-}1)^{-1}$ versus $(h\nu)^2$ of the investigated compositions can be linearly fitted in the applicability zone of the Wemple-DiDomenico, and are given in **Fig. 9 (b)**. For each plot, the fit allows the estimate of the values of both E_0 and E_d, given in **Table 3**.

Different effective medium theories are usually used to describe the dielectric constant of a composite material, which provide relationships between the packing density of the thin film and the dielectric constant. The effective medium approximation [57] is the most commonly used theory. Since its expectations are typically sensible and physically offer methods for quick knowledge into some issues that are hard to assault by different methodologies. The packing density *p* is a significant characteristic of the $(SnS)_m(Sb_2S_3)_n$ GLAD films. It can be calculated based on the effective medium approximation, and thus using the mixture rule proposed by Bruggeman:

$$p_a\left(\frac{\varepsilon_a-\varepsilon_{eff}}{\varepsilon_a+2\varepsilon_{eff}}\right)+p_b\left(\frac{\varepsilon_b-\varepsilon_{eff}}{\varepsilon_b+2\varepsilon_{eff}}\right)=0 \quad (7)$$

where ε_a and ε_b are the dielectric constants of *a* and *b* components. These components are randomly distributed in space with a packing density of p_a and p_b, respectively ($p_a + p_b = 1$). The dielectric properties of the medium are then described by the effective dielectric constant ε_{eff}. For our films, we considered that *a* component is the $(SnS)_m(Sb_2S_3)_n$ bulk material, its dielectric constant ε_a was measured directly by ellipsometry, and *b* component is the void. As a result, we considered ε_{eff} as the dielectric constant of the film. In addition, from the optical constants *n* and *k* of the GLAD films at 800 nm, packing density of different samples have systematically been calculated. Note that $SnSb_4S_7$ film exhibits the highest value of the packing density and $Sn_3Sb_2S_6$ the lowest one, which is in agreement with the SEM observations. Let's remember that these two compositions correspond to the two extreme ratio m/n in the $(SnS)_m(Sb_2S_3)_n$ formula. Usually, the packing density and the effective refractive index decrease with increasing deposition angle [30,31]. In this work, the deposition angle is fixed but the packing density depends on the composition.

3.3.5 Magneto-optical constant: Verdet coefficient V

These samples are transparent in the near infrared domain, as it is clear from the transmission spectra (**Fig.7(a)**). Therefore, they could be used as windows for applications based on magneto-optical measurements in this spectral range. The Faraday rotation is an important quantity for such measurements, and it depends on the Verdet coefficient *V* given by the following relation [58]:

$$V(\lambda) = \mu_0 r \frac{e}{2mc} \lambda \frac{dn}{d\lambda} \quad (8)$$

where μ_0 is the vacuum permeability, *r* is the magneto-optical anomaly factor, *e* is the electron charge, *m* is the electron mass, and *n* is the refractive index of the material, $dn/d\lambda$ is the dispersion of the material. Usually, for the material comprised for the most part of the covalent kind bond, *r* is near 0.28, and for the material mainly comprised of the ionic kind bond, *r* is near 1 [58]. The Verdet coefficient is normally measured using two Glan-Taylor polarizers [59,60], but in our study, we estimated it from the refractive index dispersion. We note that the Verdet coefficient takes positive and negative values, and are mainly dependent on the band gap in the negative part (**Fig.10**). This result was found for Cd-Mn-Fe-Te system, where the Verdet dispersion was negative and enhanced near the fundamental band gap energy because of the sp-d exchange interaction is enhanced [59]. In addition, in a reported work on the $Tb_2Sn_2O_7$ crystal, the Verdet constant exhibits negative values [61]. In general, the amount of heavy metals present in the sample increases the Verdet coefficient [58]. Since *V* depends on the optical dispersion, polarization and the energy splitting on the ion energy levels, the Sn addition effect in the ternary under study may be canceled by the antimony polarizability.

4. Conclusions

In this work, we investigated the structural, morphological and optical properties of the $(SnS)_m(Sb_2S_3)_n$ thin films prepared by glancing angle deposition GLAD using a single thermal

evaporation source in a vacuum. The substrates were maintained at an angle of flux incidence of 80 °. $SnSb_4S_7$, $Sn_2Sb_6S_{11}$, $SnSb_2S_4$ and $Sn_4Sb_6S_{13}$ films were firmly amorphous and $Sn_2Sb_2S_5$ and $Sn_3Sb_2S_6$ exhibit weak peaks of XRD, but their crystallinity was considered very poor. The shadowing effects and limited adatom diffusion, which inhibits the diffusivity of deposited atoms at room temperature, were the most probable cause of the amorphous character of the samples. The surface morphology was strongly dependent on the composition. The $(SnS)_m(Sb_2S_3)_n$ thin films had high absorption coefficients which reach 2×10^5 cm^{-1} in the visible range and the higher values were obtained for $Sn_3Sb_2S_6$. The shifting of the absorption edge of the films to the lower photon energy region depended on the SnS addition, and this caused a decrease of the direct band gap ($E_{g\,dir}$) and indirect band gap ($E_{g\,ind}$) from 2.11 to 1.67 eV and from 1.87 to 1.42 eV, respectively. Cauchy relation and Wemple-DiDomenico model analyzed the dispersion curves of the refractive index. The Bruggeman effective medium approximation was used to estimate the packing density *p* of different films that was determined using values of the refractive index at 800 nm. The maximum of the packing density was attributed to the $SnSb_4S_7$ (minimum of m/n) and the minimum one was for $Sn_3Sb_2S_6$ (maximum of m/n). The absorbed photo-fraction and the photocurrent were calculated for all the samples. $Sn_3Sb_2S_6$ exhibited the most important photocurrent values among the samples under study. Finally, the Verdet coefficient of the different specimens was calculated from the refractive index dispersion and it exhibited a spread negative range, which was dependent on the band gap energy.

Acknowledgment

The authors wish to express their gratitude to Dominique Demaille for SEM characterization at *Institut des NanoSciences de Paris* (INSP) and to Jérémy Bartringer at *ICube-Laboratoire des Sciences de l'Ingénieur, de l'Informatique et de l'Imagerie-France* for Raman measurement.

References

[1] Y. Hong, Y. Xing, K. Li, J. Wang, H. Pan, H. Xu, Physica E Low Dimens. Syst. Nanostruct. 60 (2014) 70-74.

[2] F. H. Siyanaki, H. R. Dizaji, M. H. Ehsani, S. Khorramabadi, Thin Solid Films 577 (2015) 128–133.

[3] B.D. Polat, O.L. Eryilmaz, R. Erck, O. Keleş, A. Erdemir, K. Amine, Thin Solid Films, 572 (2014) 134-141.

[4] B. Gallas, K. Robbie, R. Abdeddaim, G. Guida, Y. Yang, J. Rivory, A. Priou, Opt. Express 18 (2010) 16335-16344.

[5] S. Lee, W. Zhang, F. Khatkhatay, H. Wang, Q. Jia, J. L. MacManus-Driscoll, Nano Lett., 15 (2015) 7362-7369.

[6] A. Sinaoui, F. Chaffar-Akkari, B. Gallas, D. Demaille, M. Kanzari, Thin Solid Films 590 (2015) 111-117.

[7] S.Z. Rahchamani, H.R. Dizaji, M.H. Ehsani, Appl. Surf. Sci. 356 (2015) 1096-1104.

[8] N. Guth, S. Varault, J. Grand, G. Guida, N. Bonod, B. Gallas, J. Rivory, Thin solid films 571 (2014) 405-409.

[9] B.Gallas, N. Guth, J. Rivory, H. Arwin, R. Magnusson, G. Guida, J. Yang, K. Robbie, Thin solid films 519 (2011) 2650-2654.

[10] Y. Zhou, T. Taima, T. Miyadera, T. Yamanari, M. Kitamura, K. Nakatsu, Y. Yoshida, Nano Lett. 12 (2012) 4146-4152.

[11] M.M. Hawkeye, M.J. Brett, Adv. Funct. Mater 21 (2011) 3652–3658.

[12] M.M. Hawkeye, R. Joseph, J.C. Sit, M.J. Brett, Opt. Express 18 (2010) 13220-13226.

[13] M. Horprathum, K. Limwichean, A.Wisitsoraat, P. Eiamchai, K. Aiempanakit, P. Limnonthakul, N. Nuntawong, V. Pattantsetakul, A. Tuantranont, P. Chindaudom, Sens. Actuators B-Chem. 176 (2013) 685-691.

[14] M. Samadi, M. Zirak, A. Naseri, E. Khorashadizade, A. Z. Moshfegh, Thin Solid Films 605 (2016) 2-19.

[15] A. Barranco, A. Borras, A.R. Gonzalez-Elipe, A. Palmero, Prog. Mater. Sci. 76 (2016) 59-153.

[16] Y. He, J. Fu, Y. Zhao, Front. Phys. 9 (2014) 47-59.

[17] J.R. Sanchez-Valencia, R. Longtin, M.D Rossell, P. Groening, ACS Appl. Mater. Interfaces 8 (2016) 8686–8693.

[18] P-Y. Wang, D.T. Bennetsen, M. Foss, T. Ameringer, H. Thissen, P. Kingshott, ACS Appl. Mater. Interfaces 7 (2015) 4979-4989.

[19] S.M. Haque, K.D. Rao, S. Tripathi, R. Dea, D.D. Shinde, J.S. Misal, C. Prathap, M. Kumar, U. Deshpande, N.K. Sahoo, Surf. Coat. Technol. 319 (2017) 61-69.

[20] J-W. Lee, S.H. Lee, H-Seok Ko, J. Kwon, J. Hyeok Park, S. Min Kang, N. Ahn, M. Choi, J. Kyu Kim, N-G. Park, J. Mater. Chem. A 3 (2015) 9179-9186.

[21] F. Javier Ramos, M. Oliva-Ramirez, M. Khaja Nazeeruddin, M. Grätzel, A.R. González-Elipe, S. Ahmad, J. Mater. Chem. A 3 (2015) 13291-13298.

[22] S. Maidul Haque, K. Divakar Rao, J.S. Misal, R.B. Tokas, D.D. Shinde, J.V. Ramana, Sanjay Rai, N.K. Sahoo, Appl. Surf. Sci. 353 (2015) 459-468.

[23] M. Yoon, S. Lee, D. Lee, J. Kim, J. Moon, Appl. Surf. Sci. 412 (2017) 537-544.

[24] J. B. Oliver, C. Smith, J. Spaulding, A. L. Rigatti, B. Charles, S. Papernov, B. Taylor, J. Foster, C. W. Carr, R. Luthi, B. Hollingsworth, D. Cross, Opt. Mater. Express 6 (2016) 2291-2303.

[25] F. Cha□ar Akkari, D. Abdelkader, B. Gallas, M. Kanzari, Mater. Sci. Semicond. Process. 71 (2017) 156–160.

[26] A. Pareek, R. Thotakuri, R. Dom, H. Gyu Kim, P.H. Borse, Int. J. Hydrogen Energy 42 (2017) 125-132.

[27] C.H. Suena, D. Shib, Y. Suc, Z. Zhanga, C.H. Chana, X. Tangd, Y. Lic, K.H. Lamb, X. Chena, B.L. Huangc, , X.Y. Zhoud, J-Y. Dai, J. Materiomics 3 (2017) 293-298.

[28] M.R. Sazideh, H. Rezagholipour Dizaji, M.H. Ehsani, R. Zarei Moghadam, Appl. Surf. Sci. 405 (2017) 514-520.

[29] A. Sinaoui, I. Trabelsi, F. Chaffar Akkar, F. Aousgi, M. Kanzari, Int. J. Thin Fil. Sci. Tec. 3 (2014) 19-25.

[30] A. Harizi, A. Sinaoui, F. Chaffar Akkari, M. Kanzari, Mater. Sci. Semicond. Process. 41 (2016) 450-456.

[31] A. Larbi, F. Chaffar Akkari, H. Dahman, D. Demaille, B. Gallas, M. Kanzari, J. Electron. Mater. 45 (2016) 5487-5496.

[32] Z. Wang, P.R. West, X. Meng, N. Kinsey, V. M. Shalaev, A. Boltasseva, MRS Communications 6 (2016) 17-22.

[33] Y. Ma, F. Liu, M. Zhu, J. Liu, H-Hua Wang, Y. Yang, Y. Li, Nanotechnology 20 (2009) 275201.

[34] D. Abdelkader, M. Ben Rabeh, N. Khemiri, M. Kanzari, Mater. Sci. Semicond. Process. 21 (2014) 14-19.

[35] D. Sharma, S.K. Thakur, Philos. Mag. 91 (2011) 899-907.

[36] W.E. Smith, G. Dent, Modern Raman Spectroscopy – A Practical Approach, Wiley, England, 2005.

[37] D. Bougeard, Infrared and Raman spectroscopy: methods and applications, VCH, Weinheim, 1995.

[38] D. Abdelkader, F. Chaffar Akkari, N. khemiri, B. Gallas, F. Antoni, M. Kanzari, J. Alloys Compd. 646 (2015) 1049-1057.

[39] Y. Wu, Z. Xia, Z. Liang, J. Zhou, H. Jiao, H. Cao, X. Qin, Opt. Express 22 (2014) 1292-1302.

[40] L. Yang, Y. Liu , Y. Wang, W. Chen, Q. Chen, J. Wu, A. Kuznetsov, X. Du, Sol. Energ. Mat. Sol. 166 (2017) 121–126.

[41] Y. Jiang, H. Shen, T. Pu, C. Zheng , Q. Tang, K. Gao, J. Wu, C. Rui, Y. Li, Y. Liu, Sol. Energy 142 (2017) 91-96.

[42] J. Tauc, Mater. Res. Bull 3 (1968) 37-46.

[43] P. Kutálek, L. Tichy, Thin Solid Films 619 (2016) 336-341.

[44] M. Behera, S. Behera, R. Naik , RSC Adv. 7 (2017) 18428-18437.

[45] P. Pradhan, R. Naik, N. Das, A. K. Panda, AIP Conf. Proc. 1832 (2017) 080001.

[46] M.A. Alvi, Z.H. Khan, Nanoscale Res. Lett. 8 (2013) 148-158.

[47] R. Chauhan, A.K. Srivastava, A. Tripathi, K.K. Srivastava, Prog. Nat. Sci. 20 (2010) 54-60.

[48] E. Turan, M. Kul, A.S. Aybek, M. Zor, J. Phys. D: Appl. Phys. 42 (2009) 245408.

[49] M. Khadraoui,R. Miloua, N. Benramdane, A. Bouzidi, K. Sahraoui, Mater. Chem. Phys. 169 (2016) 40-46.

[50] F .Boukabrine, F. Chiker, R. Miloua, Z. Kebbab, R. Khenata, D. Prakash, S. Bin Omran, K.D. Verma, Opt. Mater. 54 (2016) 200-206.

[51] R. Swanepoel, J Phys E: Sci. Instrum. 16 (1983) 1216-1222.

[52] A.S. Hassanien, A.A. Akl, J. Alloys Compd. 648 (2015) 280-290.

[53] A.A.A. Darwish, M. Rashad, A.E. Bekheet, M.M. El-Nahass, J. Alloys Compd. 709 (2017) 640-645.

[54] M.M. El-Nahass, A. Saleh Abdul-Basit, A.A.A. Darwish, M.H. Bahlol, Opt. Commun. 285 (2012) 1221-1224.

[55] M.I. Medina-Montes, Z. Montiel-González, N.R. Mathews, X. Mathew, J. Phys. Chem. Solids 111 (2017) 182-189.

[56] S.H. Wemple, M. DiDomenico, Phys. Rev. B 3 (1971) 1338-1351.

[57] D.A.G. Bruggeman, Ann. Phys. 24 (1935) 636–643.

[58] Y. Wang, S. Wang, S. Deng, J. Liu, J. Zhang, Opt. Mater. 72 (2017) 341-345.

[59] Y. Hwang, H. Kim, S. Cho, T, Kim, Y. Um, H. Park, G. Jeen, J. Magn. Magn. Mater. 304 (2006) 309-311.

[60] Z. Chen, L. Yang, X. Wang, Y. Hang, Opt. Mater. 62 (2016) 475-478.

[61] F.Y. Guo, Q.P. Wan, Y. Hou, L.Z. Zhang, H. Fu, J.Z. Chen, J. Cryst. Growth 397 (2014) 19-23.

Captions for Tables and Figures

Table 1: Heat of atomization, RMS, threshold, number of pores in a sample surface 1 µm² and values of direct and indirect band gap energy of $(SnS)_m(Sb_2S_3)_n$ materials deposited by GLAD.

Table 2: The fitting analysis parameters of the experimental Raman spectra.

Table 3: Cauchy parameters n_0, A and B, Wemple-DiDomenico parameters the oscillator energy E_0, dispersion energy parameter E_d.

Table 4: The values of dielectric constant ε_{eff} of GLAD samples, ε_{bulk} of the bulk at λ = 800 nm and the corresponding packing density.

Fig.1: Cross-sectional (left) and surface morphology (right) SEM images of $(SnS)_m(Sb_2S_3)_n$ glancing angle deposited films.

Fig.2: (a) AFM topographic and porosity threshold images and (b) roughness histograms of $(SnS)_m(Sb_2S_3)_n$ films.

Fig.3: Schematic illustration of the thickness gradient films elaboration.

Fig.4: (a) XRD patterns and (b) Raman spectra of $(SnS)_m(Sb_2S_3)_n$ glancing angle deposited films compared with (c) Raman spectra of $(SnS)_m(Sb_2S_3)_n$ normally deposited.

Fig.5: Line focus Raman cartography and the variation of the intensity at 105 cm^{-1} as a function of X position taken in the direction of the thickness gradient.

Fig.6: The Gaussian decomposition of the Raman spectra of $(SnS)_m(Sb_2S_3)_n$ glancing angle deposited films.

Fig.7: (a) Reflectance and transmittance (b) absorption coefficients (c) $(\alpha h\nu)^2$ and (d) extinction coefficients spectra of $(SnS)_m(Sb_2S_3)_n$ glancing angle deposited films.

Fig.8: (a) Absorbed photo fraction and (b) photocurrent vs film thickness.

Fig.9: (a) Refractive indices and Cauchy fit and (b) plots of $(n^2-1)^{-1}$ versus photon energy squared $(h\nu)^2$ of $(SnS)_m(Sb_2S_3)_n$ glancing angle deposited films.

Fig.10: Verdet coefficient dispersion of $(SnS)_m(Sb_2S_3)_n$ glancing angle deposited films.

m/n	Chemical compound	H_s(kJ.mol^{-1})

	Sn	302					
	Sb	262	RMS (nm)	Threshold (nm)	Number of pores in 1 µm²	$E_{g\ dir}$ (eV)	$E_{g\ ind}$ (eV)
	S	279					
1/2	$SnSb_4S_7$	275.25	1.64	6.370	218	2.11	1.87
2/3	$Sn_2Sb_6S_{11}$	276.05	1.71	7.434	219	2.09	1.86
1/1	$SnSb_2S_4$	277.43	1.73	8.316	264	2.05	1.82
4/3	$Sn_4Sb_6S_{13}$	278.57	1.71	9.986	307	2.04	1.81
2/1	$Sn_2Sb_2S_5$	280.33	3.96	15.339	107	1.70	1.42
3/1	$Sn_3Sb_2S_6$	282.18	5.35	25.419	392	1.67	1.48

Table 1: Heat of atomization, RMS, threshold, number of pores in a sample surface 1 µm² and values of direct and indirect band gap energy of $(SnS)_m(Sb_2S_3)_n$ materials deposited by GLAD.

Table 2: The fitting analysis parameters of the experimental Raman spectra.

Composition	Peak	Area (a. u×cm^{-1})	Peak position (cm^{-1})	Width W (cm^{-1})	Baseline offset (a. u)
$SnSb_4S_7$	1	74,683	295.89	99.989	115.29
	2	5,907.2	220.87	53.272	
	3	15,803	125.51	40.078	
	4	14,620	165.45	49.354	
	5	11,418	96.16	24.564	
	6	7,070.2	77.88	15.790	
	7	2,884.7	67.69	10.800	
$Sn_2Sb_6S_{11}$	1	4,797.6	323.76	44.344	188.85
	2	26,661	309.74	85.132	
	3	17,560	277.82	74.323	
	4	19,860	233.45	111.360	
	5	21,084	135.50	59.304	
	6	10,978	94.64	27.601	
	7	6,002.6	74.18	14.869	
$SnSb_2S_4$	1	18,637	313.01	18637	138.82
	2	14,193	292.56	90.668	
	3	14,211	246.88	79.087	
	4	9,329.6	158.56	52.207	
	5	9,772.3	119.68	42.879	
	6	5,972.6	94.89	22.244	
	7	5,434.2	74.69	15.886	
$Sn_4Sb_6S_{13}$	1	26,279	312.44	67.382	164.18
	2	14,862	246.10	61.034	
	3	10,499	160.23	59.787	
	4	5,919.0	121.99	37.199	
	5	5,608.6	97.69	21.268	
	6	3,267.2	80.51	13.879	
	7	2,303.3	70.44	10.924	
$Sn_2Sb_2S_5$	1	23,634	306.00	81.498	108.78
	2	10,780	227.73	51.489	
	3	3,920.0	182.19	27.675	
	4	7,789.3	148.78	36.874	
	5	6,090.3	112.62	30.759	
	6	5,748.6	92.02	19.580	
	7	3,586.1	72.49	13.048	
$Sn_3Sb_2S_6$	1	27,049	296.20	86.393	115.431
	2	9,254.4	217.12	46.822	
	3	1,915.7	183.31	17.692	
	4	11,685	152.31	42.175	
	5	5,583.1	113.04	29.180	
	6	6,512.5	91.84	18.037	
	7	3,657.2	72.35	12.606	

Table 3: Cauchy parameters n_0, A, B and C, Wemple-DiDomenico parameters the oscillator energy E_0, dispersion energy parameter E_d.

Materials	n_0	A (nm^2)	B (nm^4)	C ($\times 10^{16}$ nm^6)	E_0 (eV)	E_d (eV)
$SnSb_4S_7$	2.06442	-36985.72575	471573226296.9657	-16.741	2.409	9.099
$Sn_2Sb_6S_{11}$	2.08061	-136378.05194	315830728736.87653	-7.798	2.371	8.872
$SnSb_2S_4$	2.25955	-345877.82580	293886141418.40356	-4.125	2.445	8.686
$Sn_4Sb_6S_{13}$	2.34264	-663357.86272	648807166696.83643	-13.391	2.394	8.550
$Sn_2Sb_2S_5$	2.16865	-912305.26490	1.1747×10^{16}	-28.358	3.817	10.236
$Sn_3Sb_2S_6$	1.9762	-751225.58305	848391846867.26941	-21.474	3.757	8.685

Table 4: The values of dielectric constant ε_{eff} of GLAD samples, ε_{bulk} of the bulk at λ = 800 nm and the corresponding packing density.

Materials	ε_{eff} (λ=800 nm)	ε_{bulk} (λ=800 nm)	p
$SnSb_4S_7$	6.295	6.766	0.942
$Sn_2Sb_6S_{11}$	5.480	6.325	0.888
$SnSb_2S_4$	5.073	7.943	0.721
$Sn_4Sb_6S_{13}$	5.631	6.084	0.936
$Sn_2Sb_2S_5$	6.317	7.697	0.857
$Sn_3Sb_2S_6$	4.269	8.607	0.622

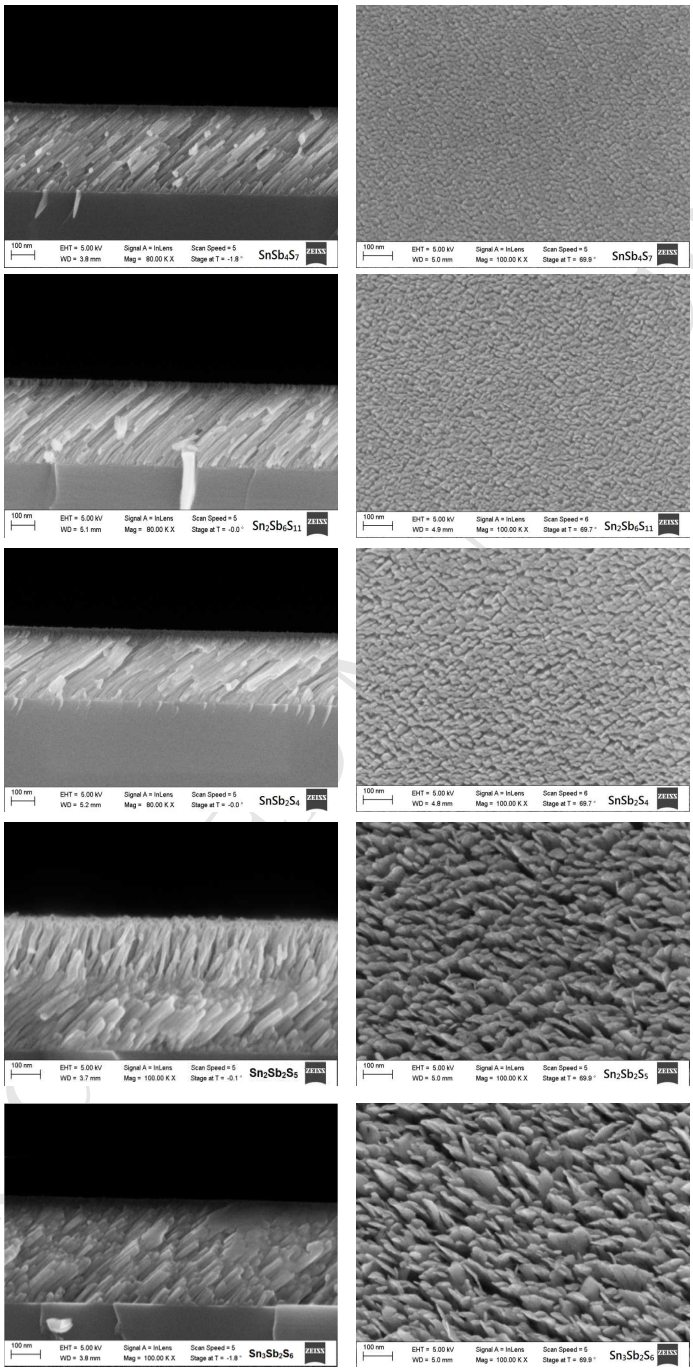
SnSb4S7
SnSb4S7
Sn2Sb6S11
Sn2Sb6S11
SnSb2S4
SnSb2S4
Sn2Sb2S5
Sn2Sb2S5
Sn3Sb2S6
Sn3Sb2S6

Fig.1

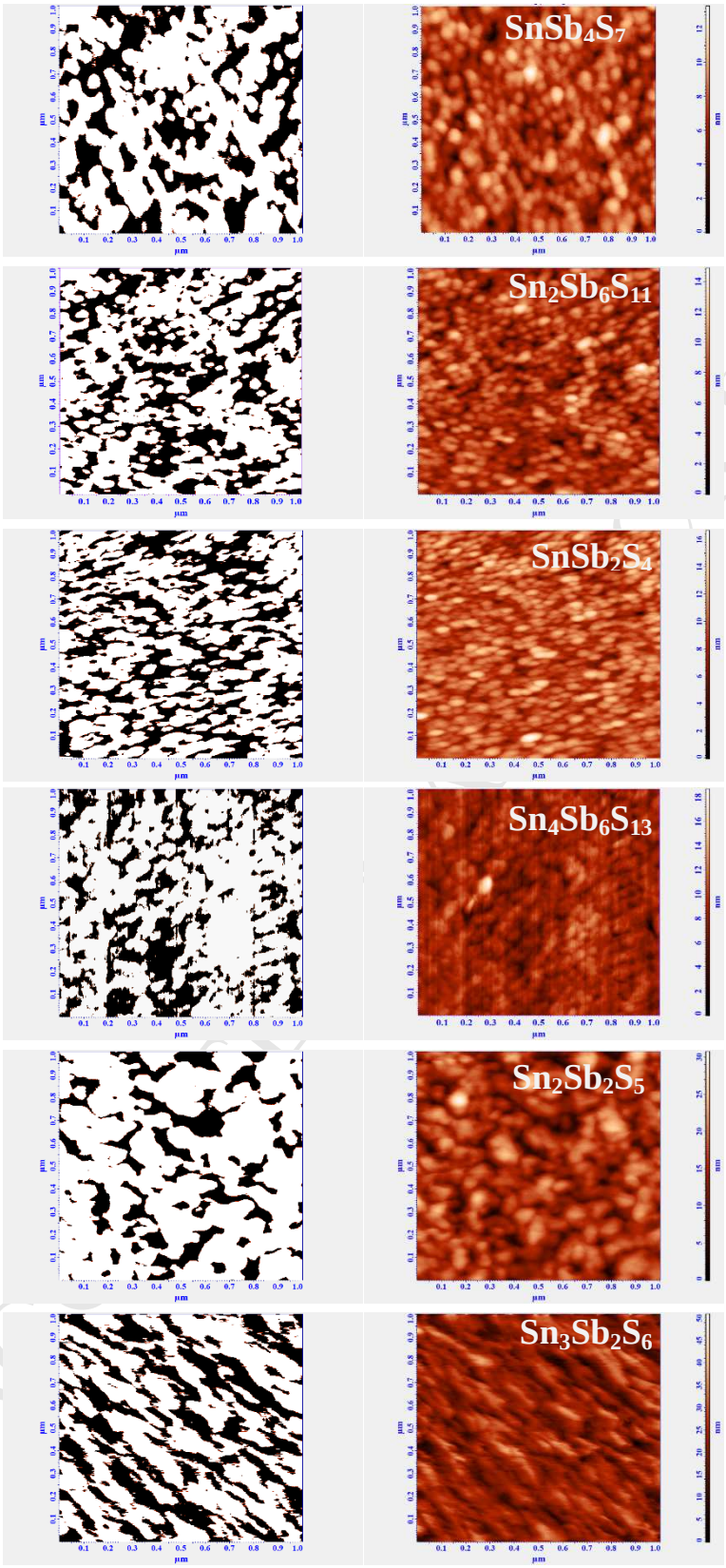

Fig.2.a

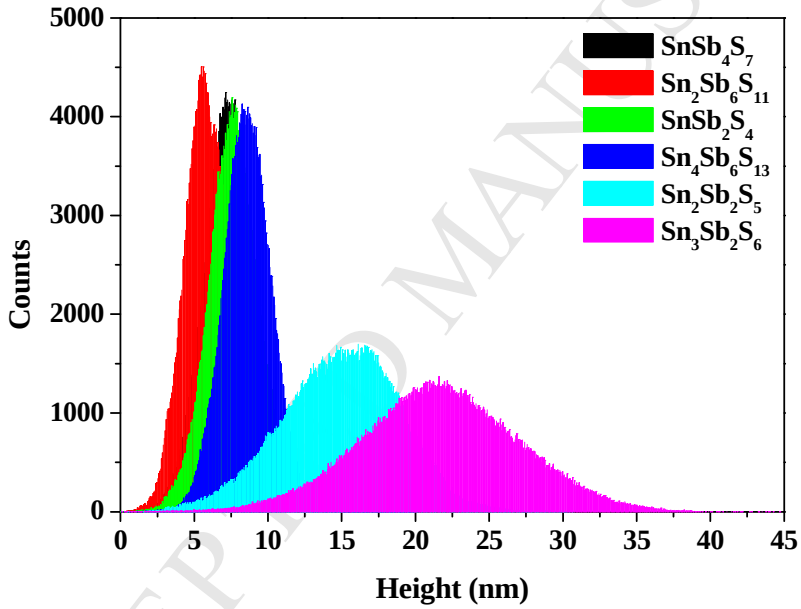

Fig.2.b

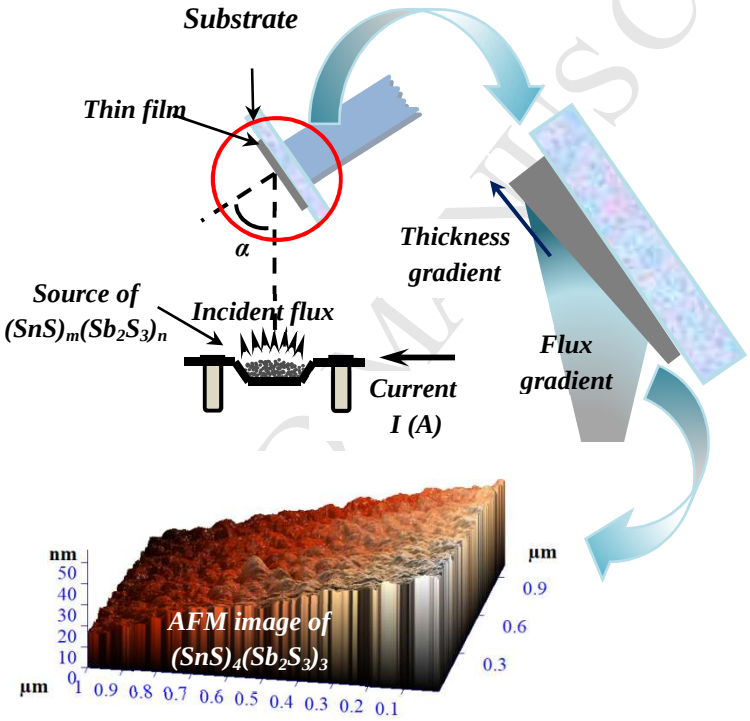
Substrate
Thin film
α
Source of
(SnS)m(Sb2S3)n
Incident flux
Current
I (A)
Thickness
gradient
Flux
gradient
nm
50
40
30
20
10
0
µm
1 0.9 0.8 0.7 0.6 0.5 0.4 0.3 0.2 0.1
µm
0.9
0.6
0.3
AFM image of
(SnS)4(Sb2S3)3

Fig.3

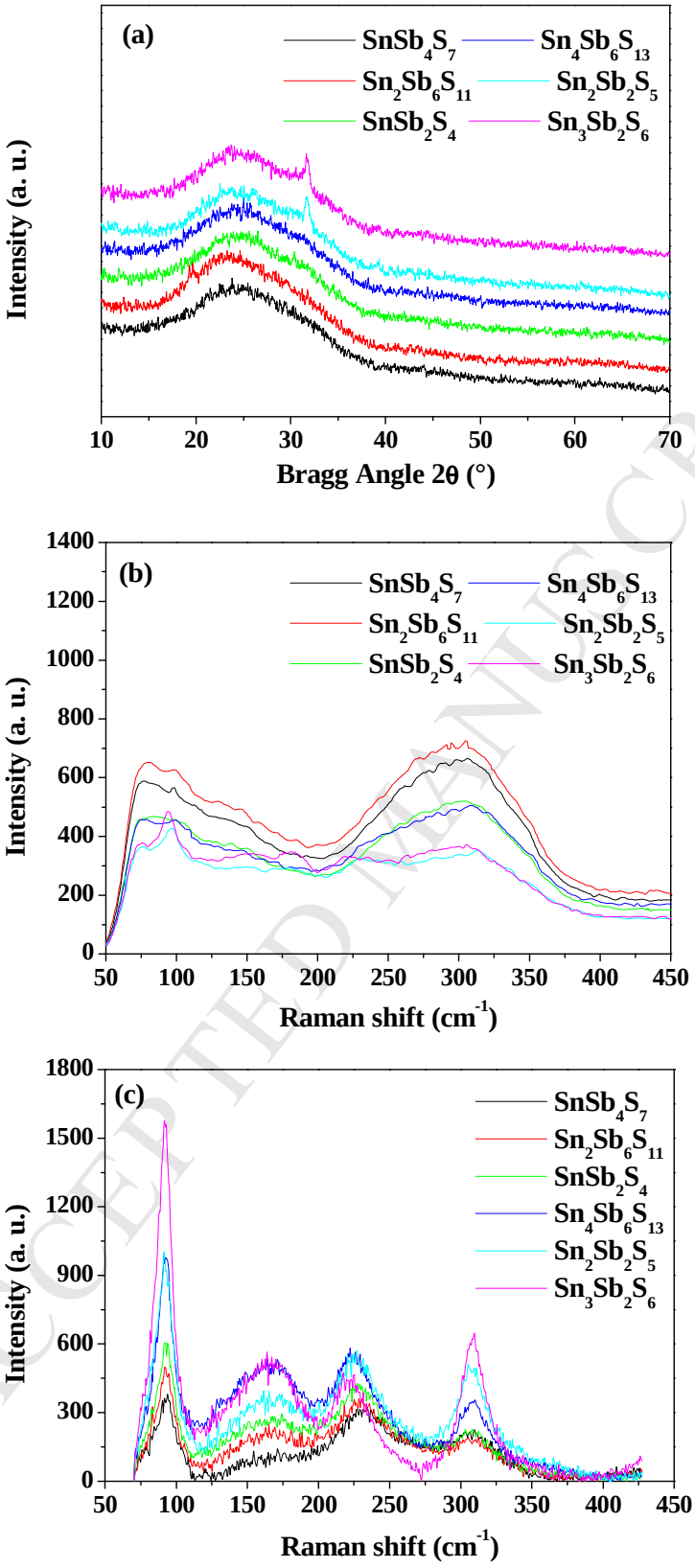
(a)
SnSb4S7
Sn4Sb6S13
Sn2Sb6S11
Sn2Sb2S5
SnSb2S4
Sn3Sb2S6
Intensity (a. u.)
Bragg Angle 2θ (°)
(b)
Raman shift (cm-1)
(c)

Fig.4

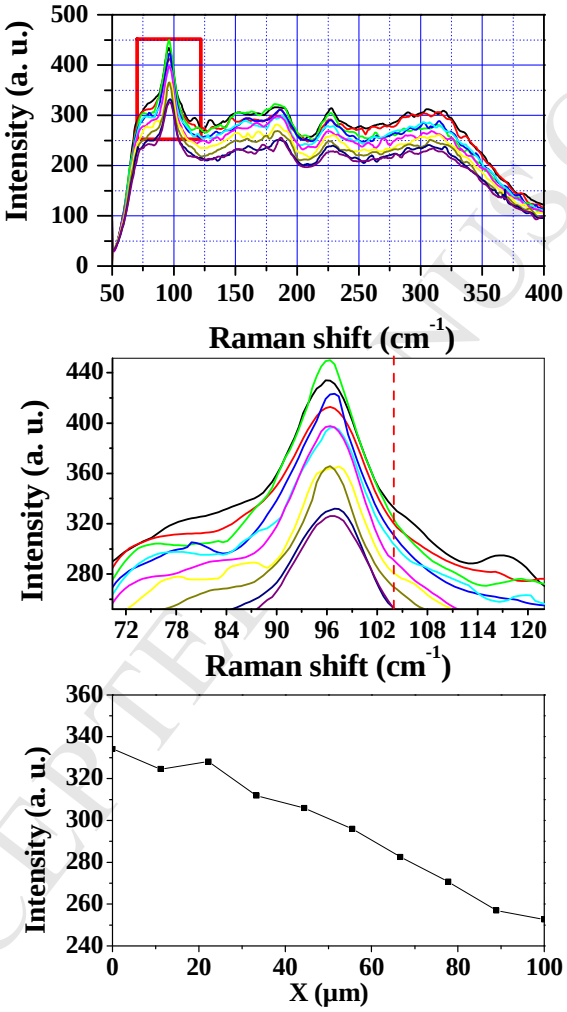
Intensity (a. u.)
500
400
300
200
100
0
50
100
150
200
250
300
350
400
Raman shift (cm-1)
Intensity (a. u.)
440
400
360
320
280
72
78
84
90
96
102
108
114
120
Raman shift (cm-1)
Intensity (a. u.)
360
340
320
300
280
260
240
0
20
40
60
80
100
X (μm)

Fig.5

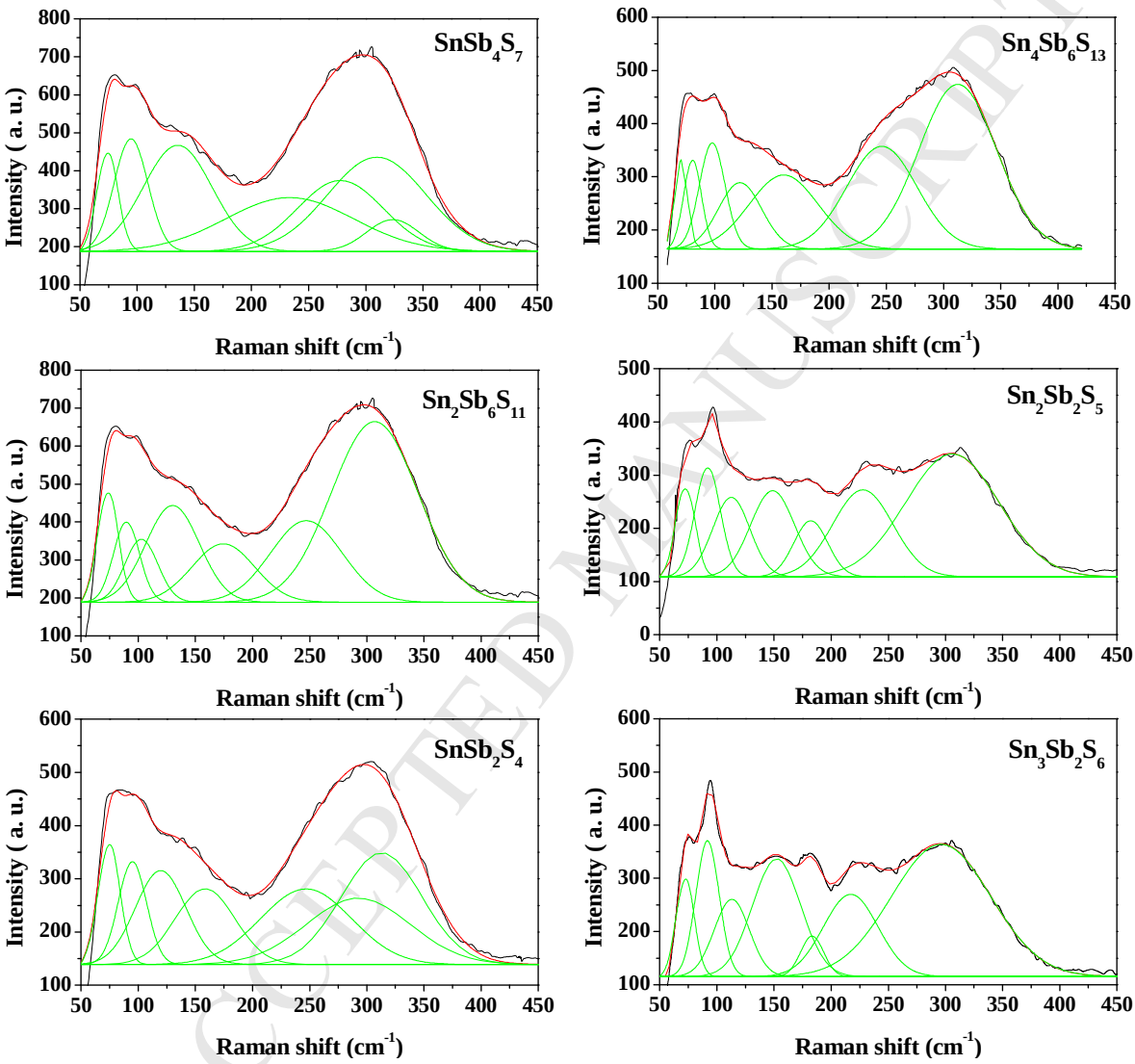
SnSb4S7
Sn4Sb6S13
Sn2Sb6S11
Sn2Sb2S5
SnSb2S4
Sn3Sb2S6
Intensity (a. u.)
Raman shift (cm-1)

Fig.6

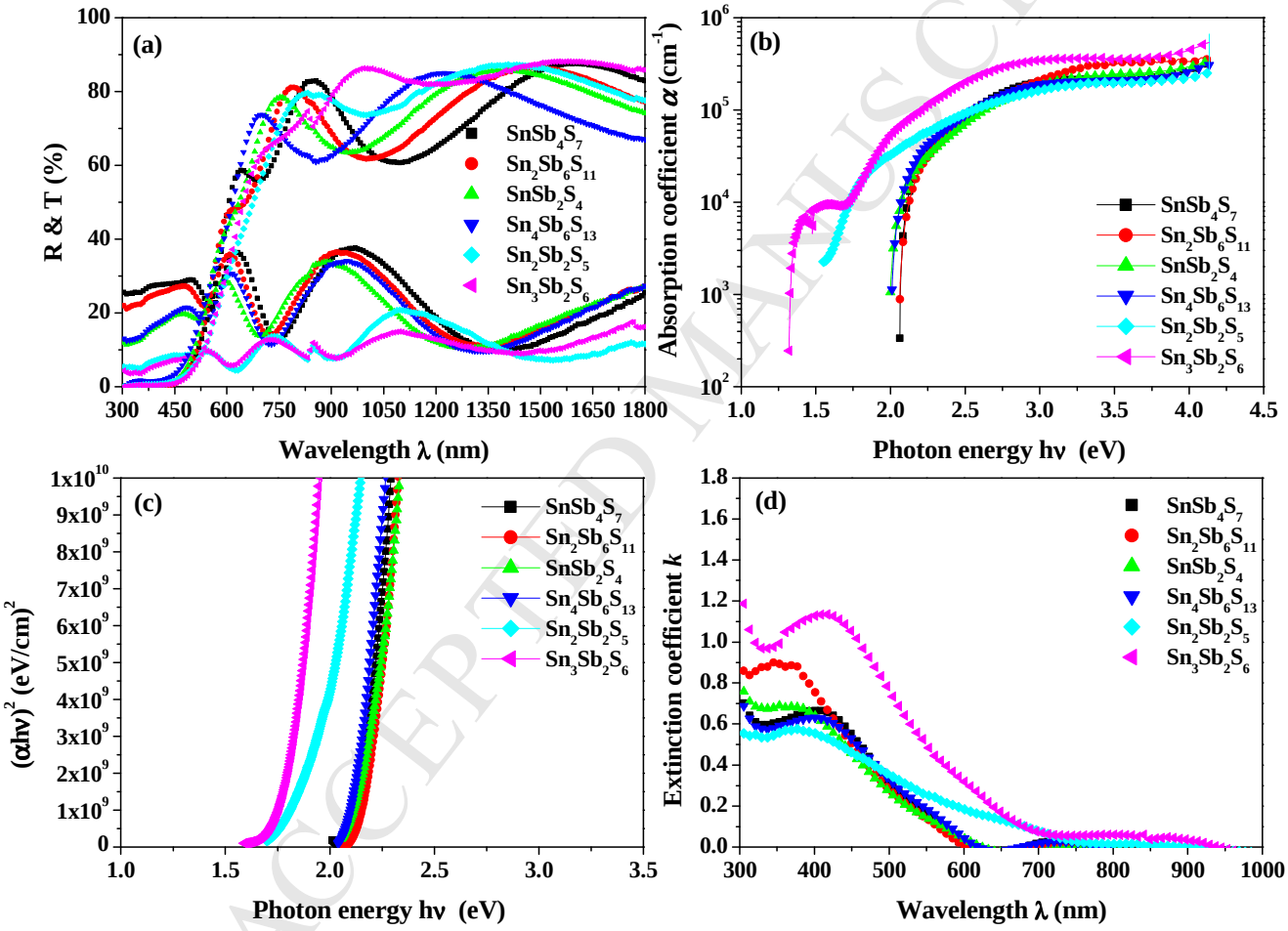
(a)
R & T (%)
Wavelength λ (nm)
(b)
Absorption coefficient α (cm-1)
Photon energy hν (eV)
(c)
(αhν)2 (eV/cm)2
Photon energy hν (eV)
(d)
Extinction coefficient k
Wavelength λ (nm)
SnSb4S7
Sn2Sb6S11
SnSb2S4
Sn4Sb6S13
Sn2Sb2S5
Sn3Sb2S6

Fig.7

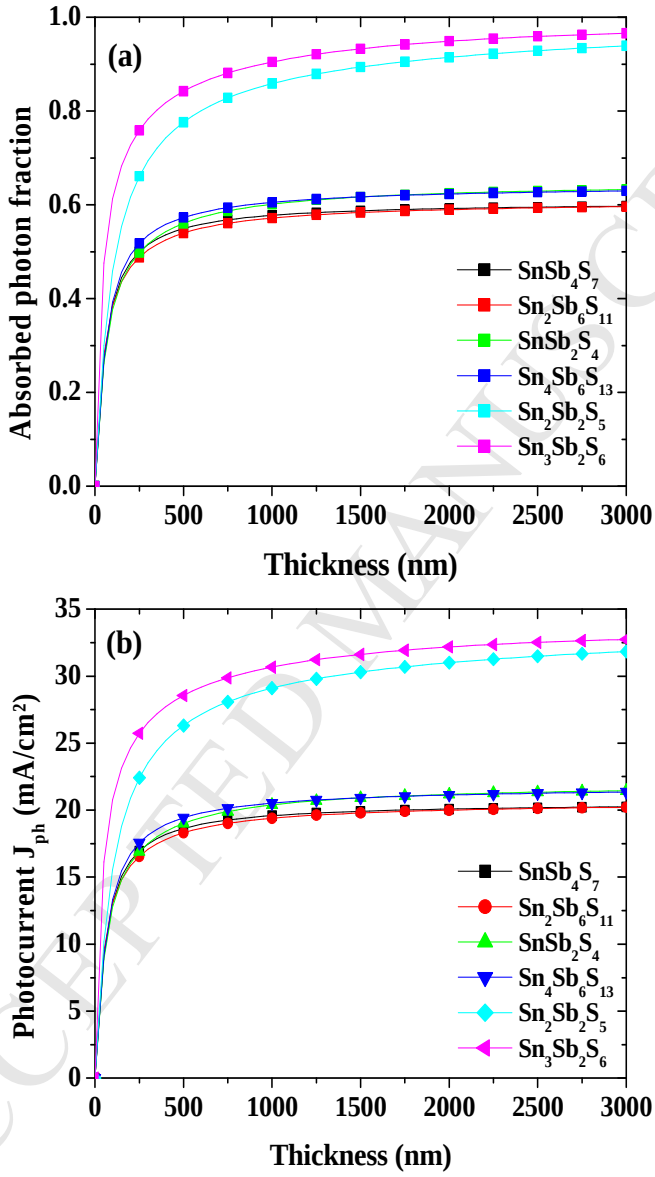
(a)
Absorbed photon fraction
Thickness (nm)
SnSb4S7
Sn2Sb6S11
SnSb2S4
Sn4Sb6S13
Sn2Sb2S5
Sn3Sb2S6
(b)
Photocurrent Jph (mA/cm2)
Thickness (nm)
SnSb4S7
Sn2Sb6S11
SnSb2S4
Sn4Sb6S13
Sn2Sb2S5
Sn3Sb2S6

Fig.8

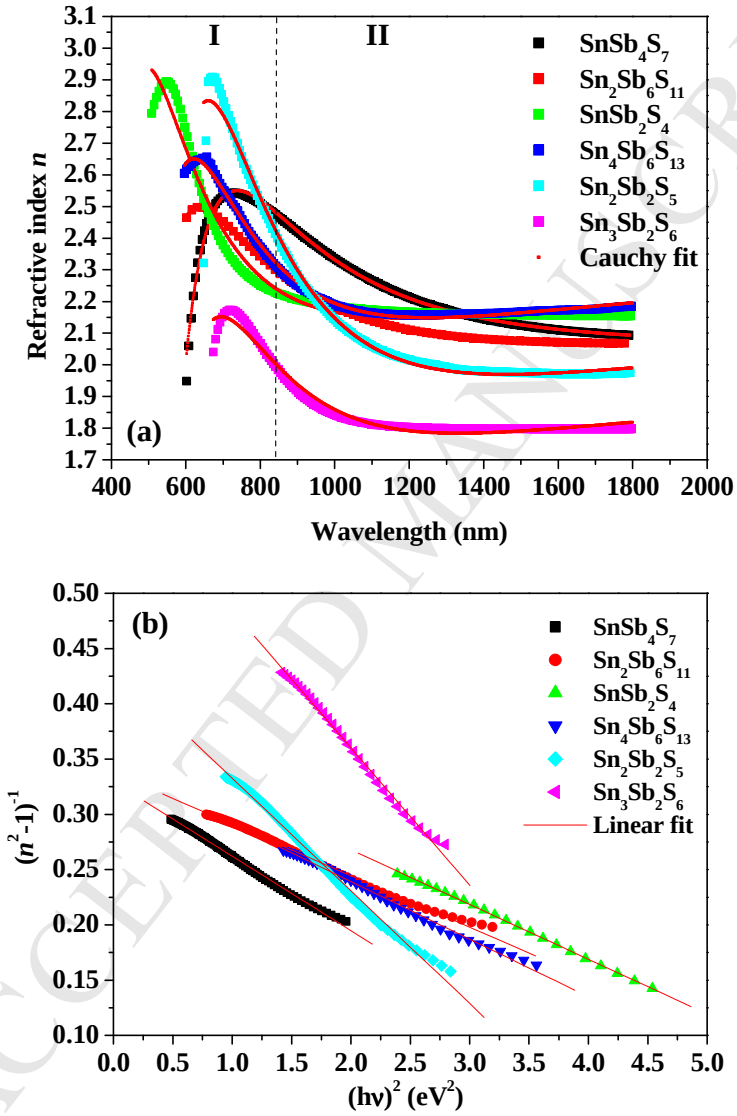
I
II
SnSb4S7
Sn2Sb6S11
SnSb2S4
Sn4Sb6S13
Sn2Sb2S5
Sn3Sb2S6
Cauchy fit
Refractive index n
Wavelength (nm)
(a)
(b)
Linear fit
(n2 -1)-1
(hν)2 (eV2)

Fig.9

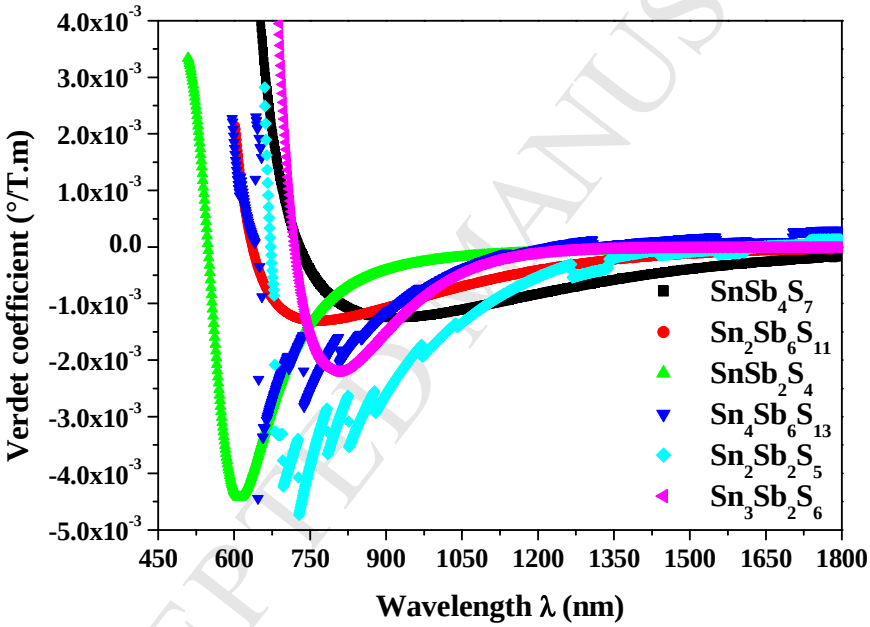

Fig.10